Aerospace Systems
https://doi.org/10.1007/s42401-020-00047-w

ORIGINAL PAPER

Dynamics and stabilization of flexible spacecraft structures with magnetic coil-pair actuators

Bryan Pawlina[1] · **Christopher J. Damaren**[1]

Received: 15 October 2019 / Revised: 6 February 2020 / Accepted: 9 March 2020

Abstract
The dynamics of flexible spacecraft structures with embedded magnetic actuators are studied. Discretized equations of motion for a constrained plate model and an unconstrained two-plate/rigid bus model are derived for actuators that create in-plane forces via current-carrying coils. Taking inputs to be the magnetic forces generated between pairs of coils, the goal of vibration suppression is shown to result in a bilinear control problem. The selection of a generalized rate output variable is used to obtain a passive map from coil-pair force inputs, yielding $\mathscr{L}_2$ stability for strictly passive feedback laws. The implementation of one such feedback corresponds to using collocated sensing at the actuator locations, and given mild assumptions about the actuator location, is a robust stabilizer with respect to unstructured uncertainties. Simulations of the closed-loop system are completed to support findings throughout.

Keywords Magnetic · Vibration · Control · Flexible · Space · Structures

1 Introduction

Flexibility is an inherent challenge for large spacecraft with extended structures. Vibration may be brought about from attitude or orbit manoeuvres, thermal stress or deployment of payloads. For vibration control, various actuation schemes have been proposed, including ways of applying transverse forces, such as with thrusters, cables or manipulators [2,5,14] control moment gyros [3,10], and piezoelectric actuators [6,15].

Magnetic control schemes have been researched for space applications in various contexts. For instance, positional control of spacecraft using the Lorentz force was studied in [9,11]. Attitude control using magnetic torques produced using current-carrying loops was studied in [8,17]. Another application explored in the latter paper is the use of electromagnetic booms to control attitude and position simultaneously. Two main problems arise in the above schemes. The first is the instantaneous underactuation arising from the cross-product force and torque laws that are inherent to external magnetic field actuation. The second is that the strength of the geomagnetic field decays with the cube of the orbit altitude. The first problem can, in some circumstances, be helped by the fact that the magnetic field in the spacecraft body frame changes as it orbits the Earth, thereby providing average controllability [16].

Arranging current-carrying conductors which produce internal structural forces to affect the vibratory behaviour of space structures was investigated in [1]. The authors conceived of magnetic coils embedded in truss elements which, when activated, served to constrain the deflection of the element, thereby altering the bending deflection by means of imposing a moment on a section of the whole structure. This arrangement leads to a linear control system. The advantages of this idea are that the coils interact with each other and, therefore, do not require a close external magnetic field, and that an electromagnetic system may be less mechanically complex, less massive, and/or higher bandwidth than another option. Our work investigates using forces as feedback laws in discrete actuator locations within continuous structures, for the particular arrangement of "coil-pairs," which are two current loops that are very close together. In contrast to the previous work, the bending deflection of the actual element in which the actuator is located is affected by the stress created by the pair of actuators.

✉ Bryan Pawlina
bryan.pawlina@mail.utoronto.ca

Christopher J. Damaren
damaren@utias.utoronto.ca

[1] University of Toronto Institute for Aerospace Studies, 4925 Dufferin Street, Toronto, Canada

Published online: 24 March 2020

The effect of the in-plane forces on the normal deflection depends on the normal deflection itself. This means that even with linearized dynamics for the attitude and elastic coordinates the controlled dynamics are bilinear. Several problems in which bilinear dynamics emerge are related to elasticity and the resulting state-dependent forcing. For instance, in [4], a thin beam with a tip-mounted electromagnet, controlled by a stationary magnet near the tip produced a bilinear system. In another example, a follower force on the end of a multibody system with flexible joints leads to a bilinear stabilization problem and was examined in [13]. Both of the above studies lead to a quadratic state feedback.

2 Magnetic coil pairs

The force between two current loops a and b is given by [1]:

$$F_{ab} = \frac{I_a I_b \mu_0}{4\pi} \oint_a \oint_b \frac{\boldsymbol{dl}_b \times (\boldsymbol{dl}_a \times (\boldsymbol{r}_a - \boldsymbol{r}_b))}{|\boldsymbol{r}_a - \boldsymbol{r}_b|^3} \tag{1}$$

where I_a, I_b are the currents in loop a and loop b respectively, $\boldsymbol{dl}_a$, $\boldsymbol{dl}_b$ are the current elements, $\boldsymbol{r}_a$, $\boldsymbol{r}_b$ are the position of the current elements, and μ_0 is the vacuum permeability. For two collinear, circular loops, sharing axis $\hat{\boldsymbol{z}}$ for their axis of symmetry, at a distance d apart, we can express the quantities in Cartesian coordinates:

$$\begin{aligned} \boldsymbol{r}_a &= [R_a \cos(\theta_a),\, R_a \sin(\theta_a),\, -d/2]^{\mathrm{T}} \\ \boldsymbol{r}_b &= [R_b \cos(\theta_b),\, R_b \sin(\theta_b),\, d/2]^{\mathrm{T}} \end{aligned} \tag{2}$$

$$\begin{aligned} \boldsymbol{dl}_a &= [-R_a \sin(\theta_a),\, R_a \cos(\theta_a),\, 0]^{\mathrm{T}} \\ \boldsymbol{dl}_b &= [-R_b \sin(\theta_b),\, R_b \cos(\theta_b),\, 0]^{\mathrm{T}} \end{aligned} \tag{3}$$

Which results in the following expression which can be numerically integrated for the force, F_{ab}:

$$F_{ab} = \frac{I_a I_b \mu_0 d R_a R_b}{4\pi} \int_0^{2\pi} \int_0^{2\pi} \times \frac{\cos(\theta_a - \theta_b)\, d\theta_a d\theta_b\, \hat{\boldsymbol{z}}}{[(R_a \cos(\theta_a) - R_b \cos(\theta_b))^2 + (R_a \sin(\theta_a) - R_b \sin(\theta_b))^2 + d^2]^{3/2}}. \tag{4}$$

The key feature is that the force can be compression or tension over a small area proportional to the product of the currents I_a and I_b, which may be controlled. Multiple rings can approximate solenoids or similar arrangements.

3 Model dynamics

3.1 Structure modelling

Consider a set of points which comprise a spacecraft $\mathscr{V}$, made of elastic parts, labeled $\mathscr{E}$, and rigid parts, labeled $\mathscr{R}$. The column matrix $\boldsymbol{r} = [x, y, z]^{\mathrm{T}}$ specifies points in the spacecraft relative to origin and coordinate frame attached to $\mathscr{R}$.

Let the small deflection of an infinitesimal mass element dm of the spacecraft, expressed in the spacecraft body frame, be given by [3]:

$$\boldsymbol{w}(\boldsymbol{r}, t) = \boldsymbol{w}_0(t) - \boldsymbol{r}^{\times}\boldsymbol{\theta}(t) + \begin{Bmatrix} \boldsymbol{u}_e(\boldsymbol{r}, t), & \boldsymbol{r} \in \mathscr{E} \\ 0, & \boldsymbol{r} \in \mathscr{R} \end{Bmatrix}, \quad \mathscr{V} = \mathscr{E} \bigcup \mathscr{R}, \tag{5}$$

where $\boldsymbol{w}_0$ is the position of the origin, $\boldsymbol{\theta}$ is the small angular deflection of $\mathscr{R}$ and $\boldsymbol{u}_e$ is the small elastic deflection of $\mathscr{E}$ with respect to $\mathscr{R}$. The skew-symmetric matrix

$$\boldsymbol{r}^{\times} = \begin{bmatrix} 0 & -z & y \\ z & 0 & -x \\ -y & x & 0 \end{bmatrix}$$

implements the cross-product operation.

The models under consideration include thin rectangular plates aligned with the body z-axis, with $z = 0$ at the mid-plane. Denoting the out-of-plane deflection by $w(x, y, t)$, the displacement field using the Kirchoff–Love assumptions is:

$$\boldsymbol{u}_e = \left[-z\frac{\partial w}{\partial x},\ -z\frac{\partial w}{\partial y},\ w \right]^{\mathrm{T}} \tag{6}$$

The expression for strain energy due to bending is given by [12]:

$$U_B = \frac{D}{2} \int_{\mathscr{E}_A} \left\{ (\nabla^2 w)^2 + 2(1-\nu) \left[\left(\frac{\partial^2 w}{\partial x \partial y} \right)^2 - \frac{\partial^2 w}{\partial x^2} \frac{\partial^2 w}{\partial y^2} \right] \right\} \mathrm{d}x\mathrm{d}y, \tag{7}$$

where $\mathscr{E}_A$ denotes the elastic area remaining to be integrated, as we have integrated through the thickness, h, of the plate, from $z = -h/2$ to $z = h/2$, and defined the flexural rigidity $D = \frac{Eh^3}{12(1-\nu^2)}$, where E is Young's Modulus and ν is Poisson's ratio (Fig. 1).

An additional contribution to the strain energy arises from in-plane stress intensities N_x, N_y and N_{xy}:

$$U_s = \frac{1}{2} \int_{\mathscr{E}_A} \left\{ N_x \left(\frac{\partial w}{\partial x} \right)^2 + N_y \left(\frac{\partial w}{\partial y} \right)^2 + 2N_{xy} \frac{\partial w}{\partial x} \frac{\partial w}{\partial y} \right\} \mathrm{d}x\mathrm{d}y. \tag{8}$$

Meanwhile, the kinetic energy stemming from the motion of all points in the vehicle is:

$$T = \frac{1}{2} \int_{\mathscr{V}} \rho(\boldsymbol{r}) \dot{\boldsymbol{w}}(\boldsymbol{r}, t)^2 \, \mathrm{d}x\mathrm{d}y \tag{9}$$

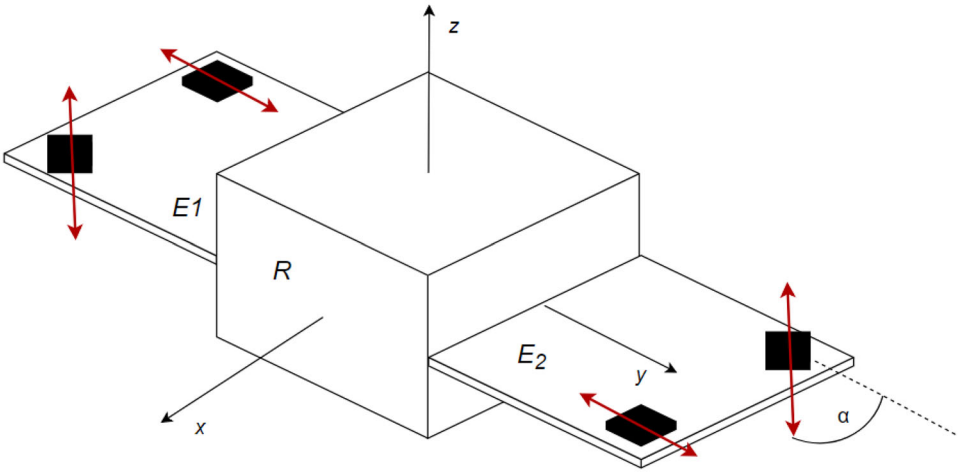

Fig. 1 Unconstrained two-plate model of rigid (R) spacecraft body with elastic (E1, E2) appendages. Red bi-arrows indicate actuator-induced stress intensities

where $\rho(\boldsymbol{r})$ is the mass density per unit area. When expanded to include rigid and elastic portions:

$$T = \frac{1}{2}\int_{\mathscr{R}} \rho_{\mathscr{R}}[\dot{\boldsymbol{w}}_0 - \boldsymbol{r}^{\times}\dot{\boldsymbol{\theta}}]^{\mathrm{T}}[\dot{\boldsymbol{w}}_0 - \boldsymbol{r}^{\times}\dot{\boldsymbol{\theta}}]\,\mathrm{d}x\mathrm{d}y + \frac{1}{2}\int_{\mathscr{E}} \rho_{\mathscr{E}}[\dot{\boldsymbol{w}}_0 - \boldsymbol{r}^{\times}\dot{\boldsymbol{\theta}} + \dot{\boldsymbol{u}}_e]^{\mathrm{T}}[\dot{\boldsymbol{w}}_0 - \boldsymbol{r}^{\times}\dot{\boldsymbol{\theta}} + \dot{\boldsymbol{u}}_e]\,\mathrm{d}x\mathrm{d}y. \tag{10}$$

To continue, the elastic deflection will be approximated using a finite set of N_e-shaped functions $\boldsymbol{\psi}_i(\boldsymbol{r})$ and associated time-varying coordinates $q_{e,i}(t)$:

$$w(x, y, t) = \sum_{i=1}^{N_e} \boldsymbol{\psi}_i(x, y) q_{e,i}(t) = \boldsymbol{\Psi}(x, y)\boldsymbol{q}_e(t). \tag{11}$$

The energies in terms of this expansion are written below. Note that differentiation of shape functions is indicated with subscripts while subscripts on N refer to stress intensity components.

$$U_B = \frac{D}{2}\int_{\mathscr{E}_A} \left\{\left[(\boldsymbol{\Psi}_{xx} + \boldsymbol{\Psi}_{yy})\boldsymbol{q}_e\right]^2 + 2(1-\nu)\left[(\boldsymbol{\Psi}_{xy}\boldsymbol{q}_e)^2 + (\boldsymbol{\Psi}_{xx}\boldsymbol{q}_e)^{\mathrm{T}}(\boldsymbol{\Psi}_{yy}\boldsymbol{q}_e)\right]\right\}\mathrm{d}x\mathrm{d}y \tag{12}$$

$$U_S = \frac{1}{2}\int_{\mathscr{E}_A} \left\{N_x\left[\boldsymbol{\Psi}_x\boldsymbol{q}_e\right]^2 + N_y\left[\boldsymbol{\Psi}_y\boldsymbol{q}_e\right]^2 + N_{xy}\left[\boldsymbol{\Psi}_x\boldsymbol{q}_e\right]^{\mathrm{T}}\left[\boldsymbol{\Psi}_y\boldsymbol{q}_e\right]\right\}\mathrm{d}x\mathrm{d}y \tag{13}$$

$$T = \frac{1}{2}\int_{\mathscr{V}} \rho(\boldsymbol{r})\left[\dot{\boldsymbol{w}}_0 - \boldsymbol{r}^{\times}\dot{\boldsymbol{\theta}} + \boldsymbol{\Psi}\dot{\boldsymbol{q}}_e\right]^{\mathrm{T}} \times \left[\dot{\boldsymbol{w}}_0 - \boldsymbol{r}^{\times}\dot{\boldsymbol{\theta}} + \boldsymbol{\Psi}\dot{\boldsymbol{q}}_e\right]\mathrm{d}x\mathrm{d}y. \tag{14}$$

We apply Hamilton's principle to determine the equations of motion

$$\delta\int_{t_i}^{t_f} [T - (U_B + U_S)]\,\mathrm{d}t = 0 \tag{15}$$

$$\int_{t_i}^{t_f} [\delta\dot{\boldsymbol{q}}^{\mathrm{T}}\boldsymbol{M}\dot{\boldsymbol{q}} - \delta\boldsymbol{q}^{\mathrm{T}}\boldsymbol{K}\boldsymbol{q}]\,\mathrm{d}t - \int_{t_i}^{t_f}\int_{\mathscr{E}_A} \delta\boldsymbol{q}_e^{\mathrm{T}}\Big\{N_x\boldsymbol{\Psi}_x^{\mathrm{T}}\boldsymbol{\Psi}_x + N_y\boldsymbol{\Psi}_y^{\mathrm{T}}\boldsymbol{\Psi}_y + N_{xy}(\boldsymbol{\Psi}_x^{\mathrm{T}}\boldsymbol{\Psi}_y + \boldsymbol{\Psi}_y^{\mathrm{T}}\boldsymbol{\Psi}_x)\Big\}\boldsymbol{q}_e\,\mathrm{d}x\mathrm{d}y\,\mathrm{d}t = 0, \tag{16}$$

where

$$\boldsymbol{M} = \begin{bmatrix} m\mathbf{1} & -\boldsymbol{c}^{\times} & \boldsymbol{P} \\ \boldsymbol{c}^{\times} & \boldsymbol{J} & \boldsymbol{H} \\ \boldsymbol{P}^{\mathrm{T}} & \boldsymbol{H}^{\mathrm{T}} & \boldsymbol{M}_{ee} \end{bmatrix},\ \boldsymbol{K} = \begin{bmatrix} \mathbf{0}\,\mathbf{0} & \mathbf{0} \\ \mathbf{0}\,\mathbf{0} & \mathbf{0} \\ \mathbf{0}\,\mathbf{0} & \boldsymbol{K}_{ee} \end{bmatrix},$$
$$\boldsymbol{q} = [\boldsymbol{w}_0^{\mathrm{T}}(t),\ \boldsymbol{\theta}^{\mathrm{T}}(t),\ \boldsymbol{q}_e^{\mathrm{T}}(t)]^{\mathrm{T}} \tag{17}$$

m is the total mass, $\boldsymbol{c}$ is the first moment of mass, and J is the moment of inertia of the undeformed spacecraft.

$$\boldsymbol{P} = \int_{\mathscr{E}} \rho_{\mathscr{E}}[0,\ 0,\ \boldsymbol{\Psi}]^{\mathrm{T}}\,\mathrm{d}x\mathrm{d}y,$$
$$\boldsymbol{H} = \int_{\mathscr{E}} \rho_{\mathscr{E}}\boldsymbol{r}^{\times}[0,\ 0,\ \boldsymbol{\Psi}]^{\mathrm{T}}\,\mathrm{d}x\mathrm{d}y,$$
$$\boldsymbol{M}_{ee} = \int_{\mathscr{E}_A} \rho_{\mathscr{E}_A}\boldsymbol{\Psi}^{\mathrm{T}}\boldsymbol{\Psi}\,\mathrm{d}x\mathrm{d}y, \tag{18}$$

$$\boldsymbol{K}_{ee} = \int_{\mathscr{E}_A} \frac{D}{2}(\boldsymbol{\Psi}_{xx}^{\mathrm{T}}\boldsymbol{\Psi}_{xx} + \boldsymbol{\Psi}_{xx}^{\mathrm{T}}\boldsymbol{\Psi}_{yy} + \boldsymbol{\Psi}_{yy}^{\mathrm{T}}\boldsymbol{\Psi}_{xx} + \boldsymbol{\Psi}_{yy}^{\mathrm{T}}\boldsymbol{\Psi}_{yy} + (1-\nu)(2\boldsymbol{\Psi}_{xy}^{\mathrm{T}}\boldsymbol{\Psi}_{xy} - \boldsymbol{\Psi}_{xx}^{\mathrm{T}}\boldsymbol{\Psi}_{yy} - \boldsymbol{\Psi}_{yy}^{\mathrm{T}}\boldsymbol{\Psi}_{xx})\,\mathrm{d}x\mathrm{d}y \tag{19}$$

In the above definition of $\boldsymbol{M}$, bending rotary inertia of the flexible portions has been neglected (terms $z^2(\frac{\partial \dot{w}}{\partial x})^2$, $z^2(\frac{\partial \dot{w}}{\partial y})^2$ arising from $\dot{\boldsymbol{u}}_e^{\mathrm{T}}\dot{\boldsymbol{u}}_e$ are considered small).

3.2 Effect of actuators

In keeping with Newton's third law, the pairs of magnetic forces generated by the coils lie in the same line of action. In addition, there is no torque on the two coils in the $\hat{z}$ direction due to the collinear arrangement of the coil pairs. As a result, each force pair generates an in-plane tension or compression with components that contribute to N_x and N_y according to the angle the actuator makes in the x–y plane. Furthermore, we assume that the inter-coil distance in actuators is much smaller than the distance between actuators and the size of the mode shapes, and so the forces N_x and N_y can be modelled as a set of Dirac delta functions at discrete locations:

$$\begin{aligned} N_x &= \sum_{i=1}^{m} u_i(t)\cos(\alpha_i)\delta_{Dirac}(\boldsymbol{r}-\boldsymbol{r}_i), \\ N_y &= \sum_{i=1}^{m} u_i(t)\sin(\alpha_i)\delta_{Dirac}(\boldsymbol{r}-\boldsymbol{r}_i),\ N_{yx}=0, \end{aligned} \tag{20}$$

where m is the number of actuators. Now, following an integration by parts on the kinetic term noting the variation is zero at the time interval endpoints, we have

$$\int_{t_i}^{t_f} \delta\boldsymbol{q}^{\mathrm{T}}\left(-\boldsymbol{M}\ddot{\boldsymbol{q}} - \boldsymbol{K}\boldsymbol{q} - \sum_{i=1}^{m} u_i(t)\boldsymbol{\Pi}_i\boldsymbol{q}\right)\mathrm{d}t = 0 \tag{21}$$

Since the variation $\delta\boldsymbol{q}$ is arbitrary within kinematic constraints the equations of motion are

$$\boldsymbol{M}\ddot{\boldsymbol{q}} + \boldsymbol{K}\boldsymbol{q} + \sum_{i=1}^{m} u_i(t)\boldsymbol{\Pi}_i\boldsymbol{q} = 0, \tag{22}$$

where $\boldsymbol{\Pi}_i$ are control influence matrices defined as

$$\boldsymbol{\Pi}_i = \begin{bmatrix} \boldsymbol{0} & \boldsymbol{0} & \boldsymbol{0} \\ \boldsymbol{0} & \boldsymbol{0} & \boldsymbol{0} \\ \boldsymbol{0} & \boldsymbol{0} & \boldsymbol{K}_{c,i} \end{bmatrix},\ \boldsymbol{K}_{c,i} = \left[\cos(\alpha_i)\boldsymbol{\Psi}_x^{\mathrm{T}}\boldsymbol{\Psi}_x + \sin(\alpha_i)\boldsymbol{\Psi}_y^{\mathrm{T}}\boldsymbol{\Psi}_y\right]\Big|_{\boldsymbol{r}=\boldsymbol{r}_i} \tag{23}$$

and α_i is the angle the actuator makes in the x–y plane.

4 Stabilization

4.1 Constrained case

Consider the case where a flexible plate is cantilevered on one side to a rigid platform. Such a system with embedded coil-pair actuators would be described by:

$$\boldsymbol{M}_{ee}\ddot{\boldsymbol{q}}_e + \boldsymbol{K}_{ee}\boldsymbol{q}_e + \sum_{i=1}^{m} u_i(t)\boldsymbol{K}_{c,i}\boldsymbol{q}_e = 0. \tag{24}$$

Matrices $\boldsymbol{M}_{ee}$ and $\boldsymbol{K}_{ee}$ are symmetric and positive definite. The Lyapunov function $V = \frac{1}{2}\dot{\boldsymbol{q}}_e^{\mathrm{T}}\boldsymbol{M}_{ee}\dot{\boldsymbol{q}}_e + \frac{1}{2}\boldsymbol{q}_e^{\mathrm{T}}\boldsymbol{K}_{ee}\boldsymbol{q}_e$ is, therefore, positive definite. Its time derivative is:

$$\dot{V} = \dot{\boldsymbol{q}}_e^{\mathrm{T}}[\boldsymbol{M}_{ee}\ddot{\boldsymbol{q}}_e + \boldsymbol{K}_{ee}\boldsymbol{q}_e] = -\dot{\boldsymbol{q}}_e^{\mathrm{T}}\left[\sum_{i=1}^{m} u_i(t)\boldsymbol{K}_{c,i}\boldsymbol{q}_e\right]. \tag{25}$$

If $u_i(t) = k_i\boldsymbol{q}_e^{\mathrm{T}}\boldsymbol{K}_{c,i}\dot{\boldsymbol{q}}_e$, where k_i is a positive constant then $\dot{V} = -\sum_{i=1}^{m} k_i\dot{\boldsymbol{q}}_e^{\mathrm{T}}\boldsymbol{K}_{c,i}\boldsymbol{q}_e\boldsymbol{q}_e^{\mathrm{T}}\boldsymbol{K}_{c,i}\dot{\boldsymbol{q}}_e$, and the equations become:

$$\boldsymbol{M}_{ee}\ddot{\boldsymbol{q}}_e + \sum_{i=1}^{m} k_i\boldsymbol{K}_{c,i}\boldsymbol{q}_e\boldsymbol{q}_e^{\mathrm{T}}\boldsymbol{K}_{c,i}\dot{\boldsymbol{q}}_e + \boldsymbol{K}_{ee}\boldsymbol{q}_e = 0 \tag{26}$$

Hence, $\dot{V}$ is negative semi-definite. If $\boldsymbol{q}_e$ is identically zero then the system is in equilibrium, and if $\dot{\boldsymbol{q}}_e = 0$, then $\ddot{\boldsymbol{q}}_e$ is also zero, and the only solution to $\boldsymbol{K}_{ee}\boldsymbol{q}_e = 0$ is the origin since $\boldsymbol{K}_{ee} > 0$. It is possible, however, for the expression $\dot{V} = -(\dot{\boldsymbol{q}}_e^{\mathrm{T}}\boldsymbol{K}_{c,i}\boldsymbol{q}_e)^2$ to be zero for non-trivial trajectories depending on the construction of $\boldsymbol{K}_{c,i}$.

To illustrate the effect of actuator placement on control influence matrices $\boldsymbol{K}_{c,i}$, the Euler–Lagrange equations are written in modal form using eigenvectors $\boldsymbol{q}_{e,\beta}$ from the unforced problem:

$$-\omega_\beta^2\boldsymbol{M}_{ee}\boldsymbol{q}_{e,\beta} + \boldsymbol{K}_{ee}\boldsymbol{q}_{e,\beta} = 0 \tag{27}$$

which satisfy the orthogonality relations

$$\boldsymbol{q}_{e,\beta}^{\mathrm{T}}\boldsymbol{M}_{ee}\boldsymbol{q}_{e,\gamma} = \delta_{\beta\gamma}, \qquad \boldsymbol{q}_{e,\beta}^{\mathrm{T}}\boldsymbol{K}_{ee}\boldsymbol{q}_{e,\gamma} = \omega_\beta^2\delta_{\beta\gamma} \tag{28}$$

Inserting the modal expansion

$$\boldsymbol{q}_e(t) = \sum_{\beta=1}^{N_e} \boldsymbol{q}_{e,\beta}\eta_\beta(t) \tag{29}$$

and left multiplying by each $\boldsymbol{q}_{e,\beta}^{\mathrm{T}}$ we get the modal equations

$$\ddot{\eta}_\beta + \omega_\beta^2\eta_\beta = -\sum_{i=1}^{m}\sum_{j=1}^{N_e} u_i(t)\boldsymbol{q}_{e,\beta}^{\mathrm{T}}\boldsymbol{K}_{c,i}\boldsymbol{q}_{e,j}\eta_j \tag{30}$$

Identifying

$$\boldsymbol{q}_{e,\beta}^{\mathrm{T}}\boldsymbol{K}_{c,i}\boldsymbol{q}_{e,j} = \cos(\alpha_i)\boldsymbol{q}_{e,\beta}^{\mathrm{T}}\boldsymbol{\Psi}_x^{\mathrm{T}}(\boldsymbol{r}_i)\boldsymbol{\Psi}_x(\boldsymbol{r}_i)\boldsymbol{q}_{e,j} + \sin(\alpha_i)\boldsymbol{q}_{e,\beta}^{\mathrm{T}}\boldsymbol{\Psi}_y^{\mathrm{T}}(\boldsymbol{r}_i)\boldsymbol{\Psi}_y(\boldsymbol{r}_i)\boldsymbol{q}_{e,j} \tag{31}$$

and defining

$$\boldsymbol{\varphi}_{x,\beta}^i = \boldsymbol{\Psi}_x(\boldsymbol{r}_i)\boldsymbol{q}_{e,\beta} \quad \boldsymbol{\varphi}_{y,\beta}^i = \boldsymbol{\Psi}_y(\boldsymbol{r}_i)\boldsymbol{q}_{e,\beta} \tag{32}$$

as the natural mode-shaped derivatives in the x- and y-directions evaluated at $\boldsymbol{r}_i$, the equations of motion are now:

$$\ddot{\eta}_\beta + \omega_\beta^2\eta_\beta = -u(t)\Big(\cos(\alpha_i)(\boldsymbol{\varphi}_{x,\beta}^i\boldsymbol{\varphi}_{x,1}^i\eta_1 + \boldsymbol{\varphi}_{x,\beta}^i\boldsymbol{\varphi}_{x,2}^i\eta_2 + \cdots + \boldsymbol{\varphi}_{x,\beta}^i\boldsymbol{\varphi}_{x,N_e}^i\eta_{N_e}) \tag{33}$$

$$+ \cdots + \sin(\alpha_i)(\boldsymbol{\varphi}_{y,\beta}^i\boldsymbol{\varphi}_{y,1}^i\eta_1 + \boldsymbol{\varphi}_{y,\beta}^i\boldsymbol{\varphi}_{y,2}^i\eta_2 + \cdots + \boldsymbol{\varphi}_{y,\beta}^i\boldsymbol{\varphi}_{y,N_e}^i\eta_{N_e})\Big) \quad \beta = 1, 2, \ldots, N_e. \tag{34}$$

We can see from the above that in order for η_β to be stabilizable, one of $\cos(\alpha)\boldsymbol{\varphi}_{x,\beta}$, $\sin(\alpha)\boldsymbol{\varphi}_{y,\beta}$ has to be non-zero. The interpretation is that the actuator must not be placed at a zero-crossing of both spatial derivatives of a mode shape. In Fig. 2, derivative nodal lines are shown for an example mode and the areas where an actuator would be ineffective in controlling that mode identified.

4.2 Unconstrained case

In the unconstrained case, we can expand the displacement using

$$\boldsymbol{q}(t) = \boldsymbol{Q}_r\boldsymbol{\eta}_r(t) + \sum_{\beta=1}^{N_e}\boldsymbol{q}_\beta\eta_\beta(t). \tag{35}$$

where $\boldsymbol{\eta}_r$ are the rigid modes, such that $\boldsymbol{K}\boldsymbol{Q}_r = \boldsymbol{0}$. A particular choice is $\boldsymbol{Q}_r = \begin{bmatrix}\boldsymbol{1}^{6\times6}\\ \boldsymbol{0}^{N_e\times6}\end{bmatrix}$ in which case $\boldsymbol{\eta}_r = [\boldsymbol{w}_{0r}(t),\ \boldsymbol{\theta}_r(t)]^{\mathrm{T}}$ are the angular and translational displacements due to the rigid modes only. The modal system equations are:

$$\begin{bmatrix} m\boldsymbol{1} & -\boldsymbol{c}^\times \\ \boldsymbol{c}^\times & \boldsymbol{J}\end{bmatrix}\ddot{\boldsymbol{\eta}}_r = 0 \tag{36}$$

$$\ddot{\eta}_\beta + \omega_\beta^2\eta_\beta = -\sum_{i=1}^{m}\sum_{j=1}^{N_e}u_i(t)\boldsymbol{q}_{e,\beta}^{\mathrm{T}}\boldsymbol{K}_{c,i}\boldsymbol{q}_{e,j}\eta_j, \quad \beta = 1, 2, \ldots, N_e. \tag{37}$$

Using a similar Lyapunov function $V = \frac{1}{2}\dot{\boldsymbol{q}}^{\mathrm{T}}\boldsymbol{M}\dot{\boldsymbol{q}} + \frac{1}{2}\boldsymbol{q}^{\mathrm{T}}\boldsymbol{K}\boldsymbol{q}$, which is now only semidefinite on account of $\boldsymbol{K}$, leads to $\dot{V} = -\dot{\boldsymbol{q}}^{\mathrm{T}}[\sum_{i=1}^{m}u_i(t)\boldsymbol{\Pi}_i\boldsymbol{q}]$. We can choose, similar to in (26), $u_i(t) = k_i\dot{\boldsymbol{q}}^{\mathrm{T}}\boldsymbol{\Pi}_i\boldsymbol{q}$ to obtain $\dot{V} = -\sum_{i=1}^{m}k_i\dot{\boldsymbol{q}}^{\mathrm{T}}\boldsymbol{\Pi}\boldsymbol{q}\boldsymbol{q}^{\mathrm{T}}\boldsymbol{\Pi}\dot{\boldsymbol{q}}$, and the equations of motion will be:

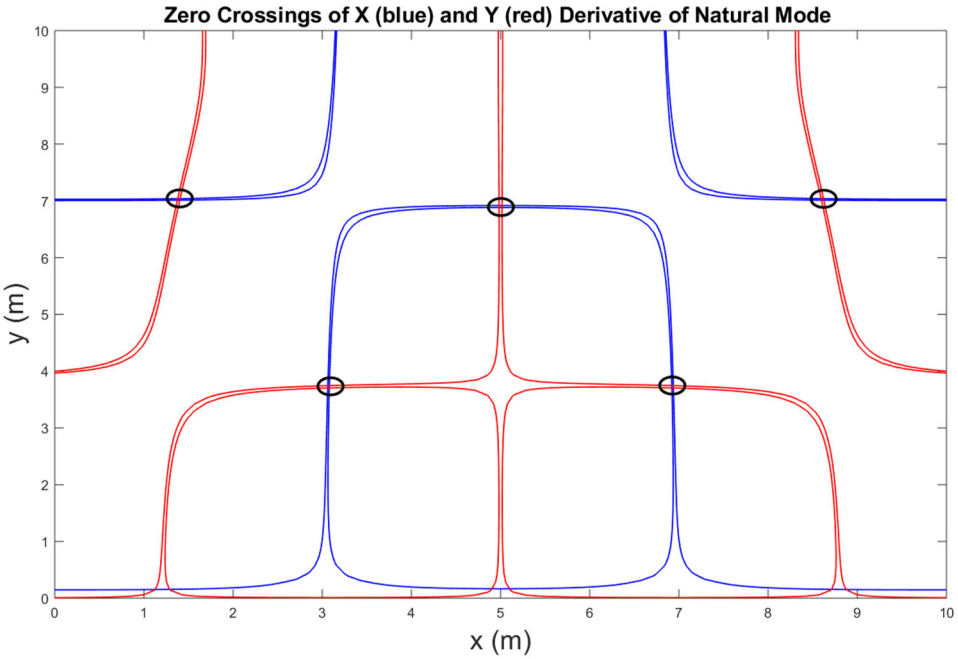

Fig. 2 x-derivative and y-derivative mode shape zero-crossings for mode with $\omega = 2.986$ rad/s. Black circles represent interior points of zero-control authority. $[L_x,\ L_y,\ \nu,\ D,\ \rho] = [10\text{ m},\ 10\text{ m},\ 0.3,\ 10\text{ Pa m}^3,\ 1\text{ kg/m}^2]$

$$\boldsymbol{M}\ddot{\boldsymbol{q}} + \sum_{i=1}^{m} k_i \boldsymbol{\Pi}_i \boldsymbol{q}\boldsymbol{q}^{\mathrm{T}} \boldsymbol{\Pi}_i \dot{\boldsymbol{q}} + \boldsymbol{K}\boldsymbol{q} = 0 \tag{38}$$

The set of trajectories the system will approach now includes linear solutions in the space of rigid body modes, as the coil-pair actuators act only on the vibration modes. Note that in this case, the eigenmodes are now based on the eigenvalue problem:

$$-\omega_\beta^2 \boldsymbol{M}\boldsymbol{q}_\beta + \boldsymbol{K}\boldsymbol{q}_\beta = 0 \tag{39}$$

and the limitations on actuator placement are based on the unconstrained modes.

4.3 Robustness and implementation

There are several advantages to analyzing these systems from the perspective of passivity. First, it may facilitate controller design beyond the Lyapunov method above. Second, it is known we can represent unmodelled vibration modes as passive mechanical systems, and so if we design a strictly passive feedback law for the controlled dynamics, it will not cause unbounded growth in the uncontrolled signals.

Shortly, we will use the partial differential equation (PDE) [12]:

$$D\nabla^2\nabla^2 w + \rho\ddot{w} = \frac{\partial}{\partial x}\left(N_x \frac{\partial w}{\partial x}\right) + \frac{\partial w}{\partial y}\left(N_y \frac{\partial w}{\partial y}\right) \tag{40}$$

Consider the positive semidefinite storage function:

$$V = \frac{1}{2}\int_{\mathscr{E}_\mathscr{A}} [D(\nabla^2 w)^2 + \rho\dot{w}^2]\,\mathrm{d}A \tag{41}$$

$$\begin{aligned}\dot{V} &= \frac{1}{2}\int_{\mathscr{E}_\mathscr{A}} \frac{\partial}{\partial t}(D(\nabla^2 w)^2 + \rho\dot{w}^2)\,\mathrm{d}A \\ &= \int_{\mathscr{E}_\mathscr{A}} [D\nabla^2 w \nabla^2 \dot{w} + \rho\dot{w}\ddot{w}]\,\mathrm{d}A \end{aligned} \tag{42}$$

$$\begin{aligned}\dot{V} = \int_{\mathscr{E}_A} [D\nabla^2(\nabla^2 w)\dot{w} + \rho\ddot{w}\dot{w}]\,\mathrm{d}A + \oint_{\partial\mathscr{E}_A} \nabla^2 w \frac{\partial \dot{w}}{\partial n}\mathrm{d}s \\ - \frac{\partial \nabla w}{\partial n}\dot{w}\,\mathrm{d}s, \end{aligned} \tag{43}$$

where $n = (n_1, n_2)$ is the outward unit normal of the plate boundary and $s = (-n_2, n_1)$ is the unit vector tangent to the boundary. The boundary integral is 0 since on the cantilever side(s), $\frac{\partial \dot{w}}{\partial n} = 0$ and $\dot{w} = 0$, while on the free sides, $\nabla^2 w = 0$ and $\frac{\partial \nabla^2 w}{\partial n} = 0$ are statements of zero boundary moment and shear force, respectively. Therefore, substituting the PDE, we have:

$$\dot{V} = \int_{\mathscr{E}_A} \dot{w}\frac{\partial}{\partial x}\left(N_x \frac{\partial w}{\partial x}\right) + \dot{w}\frac{\partial}{\partial y}\left(N_y \frac{\partial w}{\partial y}\right)\mathrm{d}A. \tag{44}$$

Integrating by parts, noting that stress intensities N_x, N_y are zero at boundaries and using the sifting property of the Dirac delta function, we get:

$$\dot{V} = -\sum_{i=1}^{m}\left(\cos(\alpha_i)\frac{\partial \dot{w}}{\partial x}\frac{\partial w}{\partial x} + \sin(\alpha_i)\frac{\partial \dot{w}}{\partial y}\frac{\partial w}{\partial y}\right)\Bigg|_{\boldsymbol{r}_i} u_i. \tag{45}$$

Taking $\boldsymbol{y} = \mathrm{col}_i\left\{-\left(\cos(\alpha_i)\frac{\partial \dot{w}}{\partial x}\frac{\partial w}{\partial x} + \sin(\alpha_i)\frac{\partial \dot{w}}{\partial y}\frac{\partial w}{\partial y}\right)\Big|_{\boldsymbol{r}_i}\right\}$, the condition for passivity, $\dot{V} \le \boldsymbol{y}^{\mathrm{T}}\boldsymbol{u}$, is satisfied with strict equality. This is the most conservative case as the inequality continues to hold in systems with structural damping.

Strictly passive systems satisfy $\int_0^{\mathrm{T}} \boldsymbol{u}^{\mathrm{T}}\boldsymbol{y}\,\mathrm{d}t \ge \epsilon\int_0^{\mathrm{T}} \boldsymbol{u}^{\mathrm{T}}\boldsymbol{u}\,\mathrm{d}t$, $\epsilon > 0$, $\forall T > 0$. If $\mathscr{H}_1$ in $\boldsymbol{y} = \mathscr{H}_1\boldsymbol{u}$ is passive, and $\mathscr{H}_2$ in $\boldsymbol{u} = \mathscr{H}_2\boldsymbol{y}$ is strictly passive, then for the feedback interconnection defined by $\boldsymbol{y} = \mathscr{H}_1\boldsymbol{e} = \mathscr{H}_1(\boldsymbol{d}-\boldsymbol{u}) = \mathscr{H}_1(\boldsymbol{d}-\mathscr{H}_2\boldsymbol{y})$, $\boldsymbol{d} \in \mathscr{L}_2 \implies \boldsymbol{y} \in \mathscr{L}_2$, where $\mathscr{L}_2 = \{\boldsymbol{u}(t) : \sqrt{\int_0^\infty \boldsymbol{u}^{\mathrm{T}}\boldsymbol{u}\,\mathrm{d}t} < \infty\}$. Stabilization is achieved for any strictly passive feedback in the presence of finite energy disturbances $\boldsymbol{d} \in \mathscr{L}_2$ [7]. Importantly, the result is valid irrespective of the model parameters or number of modes modelled. The simplest strictly passive feedback $\boldsymbol{u} = -\boldsymbol{K}_d\boldsymbol{y}$, where $\boldsymbol{K}_d$ is diagonal with positive entries, corresponds to sensors and actuators collocated in the sense that they are at the same location and the sensor reads the components $w_x\dot{w}_x|_{r_i}$ and $w_y\dot{w}_y|_{r_i}$ with the appropriate scaling given the orientation α_i of the actuator. The components $\dot{w}_x$, $\dot{w}_y$ may be obtained using a rate gyro sensor, while the w_x, w_y could be obtained using a combination of rate gyro integration and strain sensor data. However, control laws involving non-diagonal $\boldsymbol{K}_d$ (sensor coupling) and dynamic feedbacks are also possible. Note that since $w_x \approx \boldsymbol{\Psi}_x\boldsymbol{q}_e$, $w_y \approx \boldsymbol{\Psi}_y\boldsymbol{q}_e$, these output feedback laws implement the state feedback laws of section 4.1 and 4.2.

5 Simulation

The shape functions must be selected to satisfy the boundary conditions for the actual displacement $\boldsymbol{u}_e$. In both the constrained and unconstrained examples to follow, the plate is cantilevered on one side and free on the others. We select for shape functions:

$$\boldsymbol{\psi}_{i=j+(k-1)n_x}(x, y) = X(x)_j Y(y)_k \tag{46}$$

where $X_j(x)$ is the j'th eigenfunction (mode) of a thin free-free beam, that is, the j'th mode of

Table 1 Physical parameters for constrained plate simulations

N_e	L_x	L_y	ρ	ν	D	f_x	f_y	α
9	5 m	10 m	1 kg/m^2	0.3	10 Pa m^3	$[0, L_x/2, L_x]$	$[L_y, 2L_y/3, L_y]$	$[9\pi/16, \pi/2, -9\pi/16]$

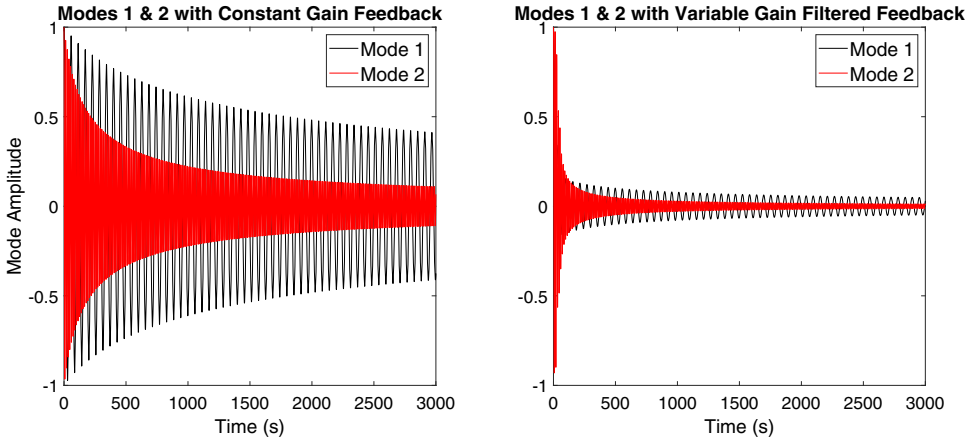

Fig. 3 Closed-loop 1st and 2nd modes with different strictly passive feedbacks for constrained model

$$\frac{\partial^4 X}{\partial x^4} - \gamma_x^4 X = 0, \quad \frac{\partial^2 X(0)}{\partial x^2} = \frac{\partial^3 X(0)}{\partial x^3} = \frac{\partial^2 X(L_x)}{\partial x^2} = \frac{\partial^3 X(L_x)}{\partial x^3} = 0 \tag{47}$$

and $Y_k(y)$ is the k'th eigenfunction of a thin cantilevered beam, satisfying

$$\frac{\partial^4 Y}{\partial y^4} - \gamma_y^4 Y = 0, \quad Y(0) = \frac{\partial Y(0)}{\partial y} = \frac{\partial^2 Y(L_y)}{\partial y^2} = \frac{\partial^3 Y(L_y)}{\partial y^3} = 0 \tag{48}$$

n_x is the number of $X_j(x)$ used in the approximation. To clarify the indexing, it is just the reordering of the matrix $[X_1\ X_2\ \ldots]^{\mathrm{T}}\,[Y_1\ Y_2\ \ldots]$ into a single vector by column concatenation. In this way, all possible products of beam-shaped functions constitute the shape functions of the plate.

The equations of motion are written in state-space form with nonlinear output:

$$\dot{\boldsymbol{x}} = \boldsymbol{A}\boldsymbol{x} + \sum_{i=1}^{m} u_i(t)\boldsymbol{B}_i\boldsymbol{x}, \quad y_i = -\boldsymbol{x}^{\mathrm{T}}\boldsymbol{\Pi}_i\boldsymbol{x}, \tag{49}$$

where

$$\boldsymbol{x} = \begin{bmatrix} \boldsymbol{q} \\ \dot{\boldsymbol{q}} \end{bmatrix}, \quad \boldsymbol{q} = \begin{bmatrix} \boldsymbol{w}_0 \\ \boldsymbol{\theta} \\ \boldsymbol{q}_e \end{bmatrix}, \quad \boldsymbol{A} = \begin{bmatrix} \boldsymbol{0} & \boldsymbol{1} \\ -\boldsymbol{M}^{-1}\boldsymbol{K} & \boldsymbol{0} \end{bmatrix},$$
$$\boldsymbol{B}_i = \begin{bmatrix} \boldsymbol{0} & \boldsymbol{0} \\ -\boldsymbol{M}^{-1}\boldsymbol{\Pi}_i & \boldsymbol{0} \end{bmatrix} \tag{50}$$

A 4th-order Runge–Kutta method is applied below to simulate the closed-loop dynamics.

5.1 Constrained case

The constrained model with embedded actuators was simulated from an initial deflection of $\eta_1(t=0) = \eta_2(t=0) = 1$. Table 1 shows the physical parameters used.

Here, f_x, f_y are the locations of the actuators. The side $y = 0$ is cantilevered, while the other three edges are free. In the left plot of Fig. 3, the control laws $u_i(t) = 1000\boldsymbol{q}_e^{\mathrm{T}}\boldsymbol{K}_{c,i}\dot{\boldsymbol{q}}_e$ N/m are used on all actuators. This is a discretized version of what might be implemented in practice with $u_i = -1000\ y_i$. Now, suppose the output is filtered to reject noise in measurement. In addition, we notice that because the model is state dependent, the controller has trouble reducing the small oscillations. We can use a steeper gain profile close to the origin as follows:

$$u_i(t) = -\left\{ \begin{array}{ll} S_1(r_i(t) - \epsilon) + \epsilon S_2, & r_i > \epsilon \\ S_2 r_i(t), & -\epsilon \le r_i \le \epsilon \\ S_1(r_i(t) + \epsilon) - \epsilon S_2, & r_i < -\epsilon \end{array} \right\}, \quad \times S_2 > S_1 \ge 0, \epsilon > 0, \tag{51}$$

where $\dot{r}_i + \lambda r_i = y_i$, $\lambda > 0$, so the controller is composed of a strictly positive real linear block (the first-order filter) connected in series with a strictly passive static nonlinearity. Such a system with an arbitrarily small feedforward $\varepsilon > 0$ is strictly passive [7]. This modified feedback with parameters $(S_1, S_2) = (1000, 2 \times 10^5)$ $\epsilon = 0.05\mathrm{s}^{-1}$, $\lambda = 3\mathrm{s}^{-1}$ is used on all actuators and shown on the right in Fig. 3.

Table 2 Physical parameters for unconstrained plate simulations

N_e	L_x	L_y	ρ	ν	D	f_x	f_y	α
2×9	10 m	10 m	1 kg/m^2	0.3	10 Pa m^3	$[0, L_x]$	$[L_y, L_y]$	$[\pi/4, -\pi/4]$ rad

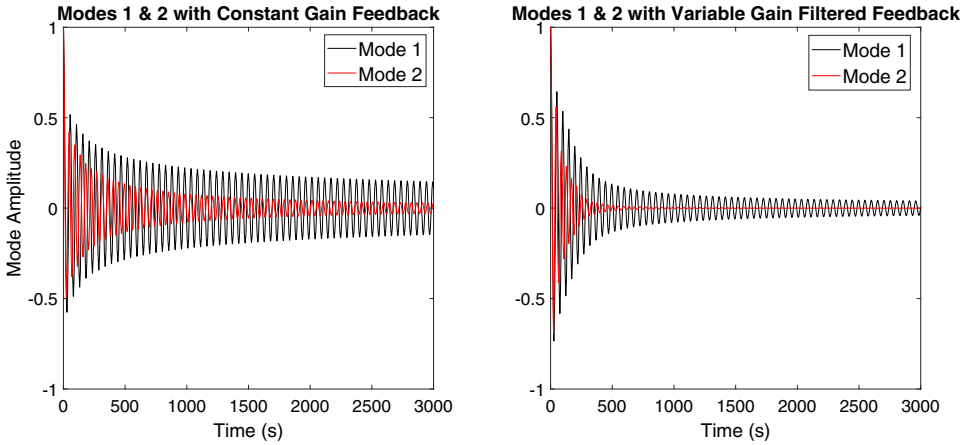

Fig. 4 Closed-loop 1st and 2nd modes with different strictly passive feedbacks for unconstrained model

5.2 Unconstrained case

The unconstrained model with embedded actuators was simulated from an initial deflection of $\eta_1(t=0) = \eta_2(t=0) = 1$. Table 2 shows the physical parameters used. The N_e field means that each plate has nine elastic degrees of freedom.

The parameters in Table 2 apply to both plates; the spacecraft and its actuators have odd symmetry in the x–y plane. The rigid body $\mathscr{R}$ has dimensions $[x_{\text{dim}},\ y_{\text{dim}},\ z_{\text{dim}}] = [10,\ 10,\ 5]$ m and mass 500 kg. On the left in Fig. 4, we have the closed-loop response for $u_i(t) = 5000\boldsymbol{q}^{\mathrm{T}}\boldsymbol{\Pi}_i\dot{\boldsymbol{q}}$, while on the right, we have the same type of variable-gain feedback as in the second constrained case with parameters $(S_1, S_2) = (1, 5 \times 10^4)$, $\epsilon = 0.0002\ \text{s}^{-1}$, $\lambda = 0.25\ \text{s}^{-1}$.

It is notable that the first mode of both the constrained and unconstrained structure persists more than the second and other higher modes, ordered by natural frequency. The reason is that the control input u_i multiplies $\boldsymbol{B}_i\boldsymbol{x}$, which is proportional to the state and, therefore, has less effect with small vibrations. The construction of $\boldsymbol{B}_i$ shows that modes with fewer nodes have generally smaller slope values, and thus smaller multipliers of the control. Therefore, the above scheme for undamped structures more readily depletes the oscillation of higher frequency modes.

6 Conclusion

We have investigated the effect of embedded coils of current carrying wire in flexible constrained and unconstrained structures. The resulting bilinear control problem has been approached first through an assignment to make the Lyapunov function negative. Next, it was shown this technique can be generalized to strictly passive feedback controllers given that a sensor measures a special output, given by x–y-components of the product of slope and slope-rate. The robustness with respect to model parameter error, unmodelled passive dynamics, and finite-energy disturbances arise naturally from the passivity-based feedback technique. The main limitation to this method is that actuators/sensors must be placed away from regions where the derivatives of the natural mode shapes are zero in both directions. Simulations show some example actuator configurations that are effective at suppressing structural vibration with these feedback laws.

References

1. Anastas G, Eisenhaure D, Hockney R, Johnson B, Misovec K (1988) Distributed magnetic actuators for fine shape control. AFAL-TR-88-026, Air Force Astronautics Laboratory, Edwards Air Force Base, California
2. Casella F, Locatelli A, Schiavoni N (2002) Modeling and control for vibration suppression in a large flexible structure with jet thrusters and piezoactuators. IEEE Trans Control Syst Technol 10(4):589–599
3. Damaren CJ, D'Eleuterio GMT (1989) Optimal control of large space structures using distributed gyricity. AIAA J Guid Control Dyn 12(5):723–731
4. Fung R-F, Wang C-C, Liu Y-T (2005) Dynamic model of an electromagnetic actuator for vibration control of a cantilever beam with a tip mass. J Sound Vib 288(4–5):957–980
5. Guo T, Lu Q, Li J (2008) PI force feedback control for large flexible structure vibration with active tendons. Acta Mech Sin 24(6):721–725 ISSN 0567-7718
6. Hu Y-R, Ng A (2005) Active robust vibration control of flexible structures. J Sound Vib 288(1):43–56 ISSN 0022-460X
7. Khalil HK (2014) Nonlinear systems, Third edn. Pearson Education, Inc, USA, pp 227–250

8. Lovera M, Astolfi A (2004) Spacecraft attitude control using magnetic actuators. Automatica 40(8):1405–1414 ISSN 0005-1098
9. Peck MA, Streetman B, Saaj CM, Lappas V (2007) Spacecraft formation flying using Lorentz forces. J Br Interplanet Soc 60(7):263–267 ISSN 0007-084X
10. Shi J-F, Damaren CJ (2005) Control law for active structural damping using a control moment gyro. J Guid Control Dyn 28(3):550–553 ISSN 0731-509
11. Silani E, Lovera M (2005) Magnetic spacecraft attitude control: a survey and some new results. Control Eng Pract 13(3):357–371
12. Shames IH, Dym CL (1985) Energy and finite element methods in structural mechanics. Hemisphere Publishing Corporation, New York, pp 432–433
13. Slemrod M (1978) Stabilization of bilinear control systems with applications to nonconservative problems in elasticity. SIAM J Control Optim 16(1):131–141
14. Tzeranis D, Dubowsky S (2006) Vibration control in the assembly of large flexible structures by teams of space robots. IFAC Proc 39(15):719–724
15. Voss T, Scherpen JMA (2014) Port-Hamiltonian modeling of a nonlinear Timoshenko beam with piezo actuation. SIAM J Control Optim 52(1):493–519 ISSN 0363-0129
16. Wiśniewski R, Blanke M (1999) Fully magnetic attitude control for spacecraft subject to gravity gradient. Automatica 35(7):1201–1214 ISSN 0005-1098
17. Wong B, Damaren CJ (2013) Satellite attitude control using electrodynamic booms. Int J Sp Sci Eng 1(1):51–63 ISSN 2048-8459